AIAA JOURNAL
Vol. 56, No. 11, November 2018

Technical Notes

Flow-Separation Control Using Sweeping Jet Actuator

Kursat Kara*
Khalifa University, Abu Dhabi 127788, United Arab Emirates
Daegyoum Kim†
Korea Advanced Institute of Science and Technology, Daejeon 34141, Republic of Korea
and
Philip J. Morris‡
Pennsylvania State University, University Park, Pennsylvania 16802

DOI: 10.2514/1.J056715

I. Introduction

IMPROVED aerodynamic designs and new aerodynamic technologies will play a vital role in improving the next-generation aircraft's performance and contribute strongly to the product cost and operability. Active flow control (AFC) is one of the promising technologies to control boundary-layer separation, mixing, and noise. In recent years, actuators for AFC and especially fluidic oscillators have received much interest. The state of the art of improving aerodynamic performance [1], AFC actuators [2], and fluidic oscillators [3] was described in recent review papers.

Fluidic actuators increase momentum in the local flowfield by fluid injection. Sweeping jet (SWJ) actuators belong to this category of actuators, and they are based on fluidic oscillators with no moving parts [2], as shown in Fig. 1. An SWJ actuator emits a continuous but spatially oscillating jet at the outlet when pressurized with a fluid [4]. The oscillations are entirely self-induced and self-sustaining. As the supplied fluid passes through the SWJ actuator, the jet attaches itself to either side due to the Coanda effect. Then, pressure increases in the feedback loop and pushes the jet to the other side. This process repeats cyclically. As a result, an oscillating jet that sweeps from one side of the exit nozzle to the other is obtained [4,5].

In the last decade, an increasing number of studies employing the SWJ actuator have been published, especially in flow-separation control. Significant aerodynamic performance improvements have been achieved using new concepts [6,7] or SWJs [5,8–19]. The SWJ actuator has been shown to be an effective and efficient tool for separation control. Nonetheless, a lack of knowledge continues regarding the actuator's properties, underlying mechanisms, and governing parameters for flow control applications [3]. Further development of SWJ actuators is needed before their deployment into actual applications.

Recent experimental [20,21] and numerical studies [21–26] on SWJ actuators in a quiescent environment showed that the SWJ actuator is a viable flow control actuator candidate due to its simple design with no moving parts and its spatially oscillating high-momentum flow output.

The objective of the present study was to numerically determine the effectiveness of an SWJ actuator in controlling flow separation. To investigate the flow structures and control mechanisms, a widely used two-dimensional (2-D) NASA hump model [27] was undertaken. The model is a Glauert/Goldschmied-type body, geometrically similar to that used by Seifert and Pack [28]. The model was mounted between two glass end-plate frames, and both leading and trailing edges were faired smoothly, and a wind-tunnel splitter plate was placed under the model as shown in Fig. 2. Low-speed flow separation on a wall-mounted hump and its control using steady suction have been studied experimentally to generate a data set for the development and evaluation of computational methods [29]. The details of the experiment are given in Greenblatt et al. [29,30] and Naughton et al. [31]. It is a nominally 2-D experiment, treated as such for the computational fluid dynamics (CFD) validation. Experimental and computational data from various Reynolds-averaged Navier–Stokes (RANS) models are available for comparison in the NASA Langley Research Center Turbulence Modeling Resource [32]. Recently, an experimental study of flow-separation control by employing round jet and SWJ was performed by Borgmann et al. [33] for a canonical hump model. They conducted a detailed baseline characterization of flap angle, reference static pressure, Reynolds number, boundary-layer trip, and aspect ratio. They provided the comparison of pressure coefficient with previous experimental studies [28,29].

In the present study, we numerically tested the performance of an SWJ actuator on flow-separation control using 2-D unsteady RANS (URANS) simulations over a wall-mounted hump model. The SWJ actuator was integrated into the wall-mounted hump model at the upstream of separation point (65% of the chord) and angled at 30 deg to the freestream direction. The interaction of the oscillation jet in this orientation with freestream and separation bubble was studied. The three-dimensional configuration that will be investigated in future studies may exhibit spanwise vortical structures as well. In the present study, however, we considered only 2-D configuration.

II. Numerical Model and Validation

The geometry of the hump imitated the upper surface of the Glauert–Goldschmied airfoil, and the computational domain was created using the description provided by Greenblatt et al. [29]. The computational domain was 2-D, and the chord length of the hump was 420 mm. The SWJ actuator was located at 65% of the chord and was angled at 30 deg to the freestream direction. The oscillating jet came out of a single exit nozzle, located to the upstream of the separation point, as illustrated in Fig. 3. In our previous studies, the fully turbulent, compressible oscillating jet flow from the SWJ actuator was investigated using three-dimensional URANS simulations [23]. The SWJ actuator geometry with an exit-nozzle throat height of $h = 6.35$ mm was reproduced from reference [22]. Because the size of the SWJ actuator geometry studied before [21–26] was larger than the maximum height of the wall-mounted hump model, the SWJ actuator geometry was scaled down by four times. It shrunk the exit-nozzle throat height from 6.35 to 1.5875 mm (0.378% of the chord length). The inlet channel height of the SWJ

Presented as Paper 2017-3041 at the 35th AIAA Applied Aerodynamics Conference, Denver, CO, 5–9 June 2017; received 12 September 2017; revision received 30 June 2018; accepted for publication 19 July 2018; published online 12 October 2018.

*Assistant Professor, Aerospace Engineering Department; kursat.kara@kustar.ac.ae. Senior Member AIAA.

†Assistant Professor, Mechanical Engineering Department; daegyoum@kaist.ac.kr.

‡Boeing/A.D. Welliver Professor of Aerospace Engineering, Department of Aerospace Engineering; pjm@psu.edu. Fellow AIAA.

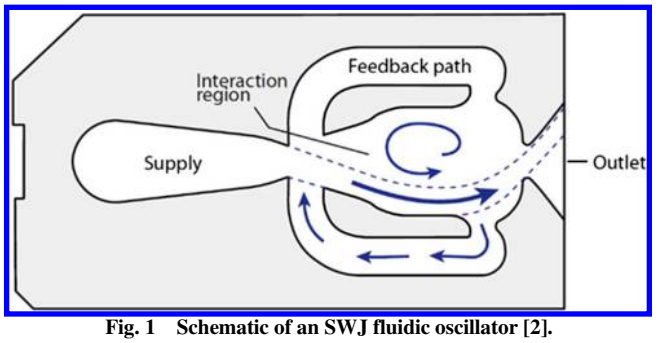

Fig. 1 Schematic of an SWJ fluidic oscillator [2].

actuator was 4.0531 mm (0.96% of the chord length). The size of the computational domain was determined from a recent study [34], and the height and length were set to $0.91c$ and $8.41c$, respectively. Similar to Fisher et al. [34], no modification was applied to the top boundary to include the effects of the end plates.

The commercial CFD software, ANSYS Fluent v17.2, which employs a control volume method to discretize the RANS equations with second-order accuracy, was used for the numerical investigation. The SIMPLE algorithm was used for pressure–velocity coupling for steady-state calculations, whereas the PISO algorithm was used for unsteady calculations with a second-order fully implicit scheme for time integration. The working fluid was air. The density was calculated from the ideal gas law. The viscosity was evaluated using Sutherland's law using the reference viscosity $\mu_0 = 1.716 \times 10^{-5}$ kg/(m · s), reference temperature $T_0 = 273.11$ K, and effective temperature $S = 110.56$ K. Similar to the experiment [29], $x/c = -2.14$ was set as the reference location for calculations. At this location, the reference pressure was set to 101,325 Pa. The inlet velocity was $V_{\text{inlet}} =$ 34.6 m/s ($M = 0.1$), normal to the boundary. A fully turbulent flow was assumed. The turbulence intensity at the inlet was 5%, and the turbulent length scale was 1 mm. The boundary and reference conditions were generated from references [29,32], and are shown in Fig. 4. The flow parameters at the inlet boundary of the 2-D NASA wall-mounted hump model are listed in Table 1. Moreover, the flow parameters at the SWJ actuator inlet boundary with varying mass-flow rates are given in Table 2.

The wall-mounted hump configuration has proved to be a challenging test case with most RANS models overpredicting the separation bubble length. However, they still give qualitatively correct solutions that are sufficient for comparative studies. A summary of recent studies employing RANS turbulence models to simulate the 2-D NASA wall-mounted hump model is given in table 1 of reference [34]. The integration of the SWJ actuator to the wall-mounted hump model increases the computational and physical complexities of the problem. Higher-fidelity simulations, such as large-eddy simulation (LES) [35], require prohibitive computational resources if a large number of cases are to be solved. Therefore, the 2-D URANS simulation approach was adopted in the present study to keep the computational cost at an affordable level. It should be noted that the present study intended to make an initial quantitative performance prediction of the SWJ actuator for the separated flow over the widely used 2-D NASA wall-mounted hump model. The present study is a conceptual exploration study similar to the case in reference [34], and further investigation using three-dimensional higher-fidelity simulations is necessary to understand the detailed flow mechanisms.

In an earlier study [22], an unsteady numerical analysis of an SWJ actuator was performed to develop an understanding of internal flow oscillations using the realizable $k-\varepsilon$ and the *shear-stress transport* (SST) $k-\omega$ turbulence models. The SST $k-\omega$ model predicted the

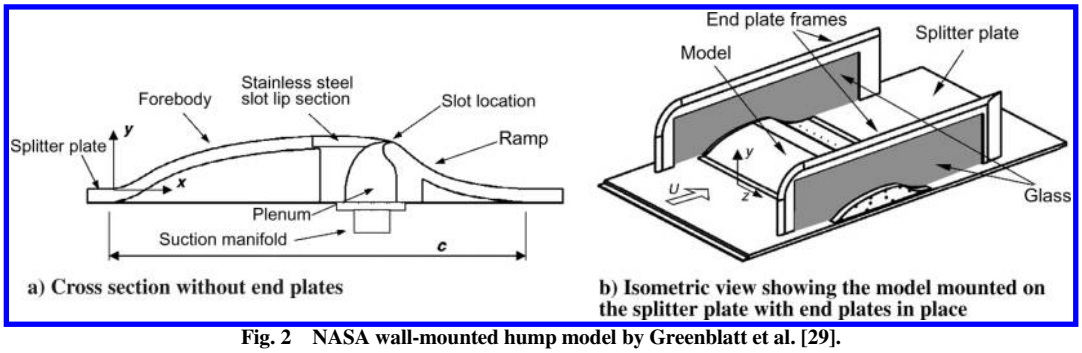

Fig. 2 NASA wall-mounted hump model by Greenblatt et al. [29].

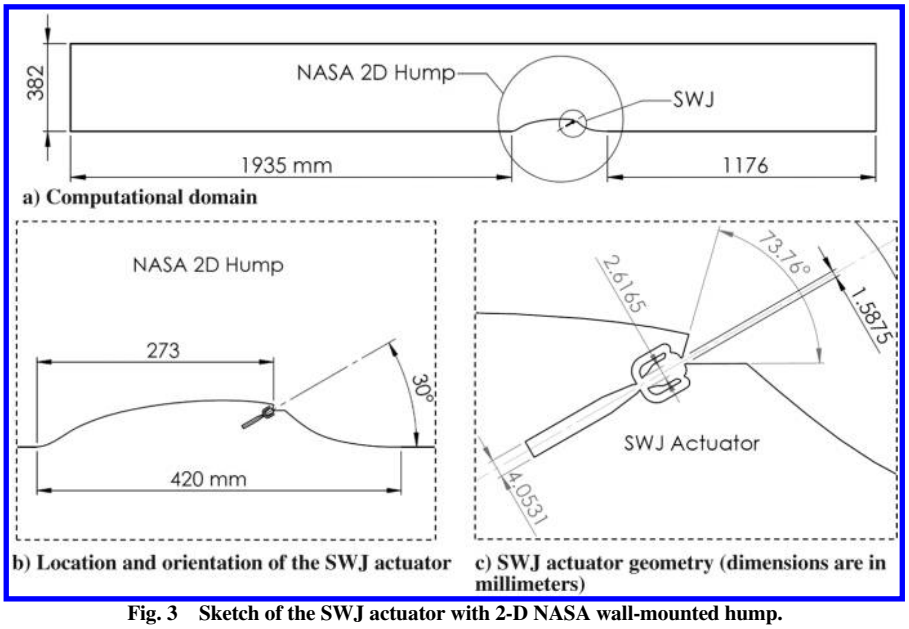

Fig. 3 Sketch of the SWJ actuator with 2-D NASA wall-mounted hump.

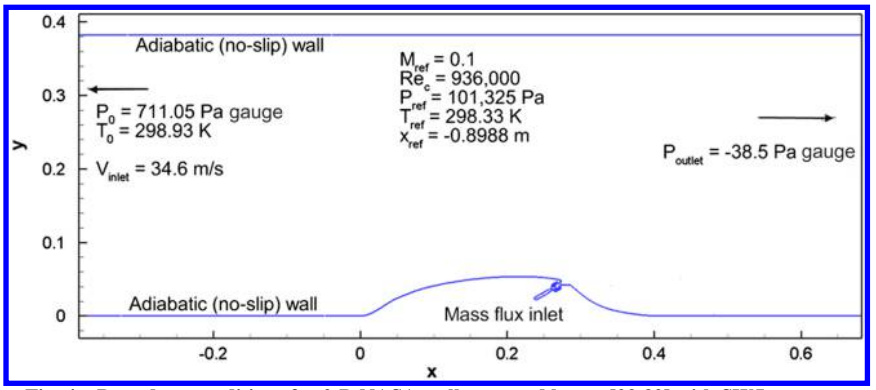

Fig. 4 Boundary conditions for 2-D NASA wall-mounted hump [29,32] with SWJ actuator.

jet velocity profiles better than the realizable $k-\varepsilon$ model. Therefore, in the present study, the SST $k-\omega$ model was used for unsteady simulations.

For unsteady analyses, the time-step size was set to $\Delta t = 1\times10^{-5}$ s (71 time steps per jet oscillation cycle for $\dot{m} = 268$ g/s) to capture the oscillating jet from the SWJ actuator. The solution did not change with a further reduction of the time step. Previous studies showed that decreasing the mass-flow rate decreases the jet oscillation frequency [23], and therefore, the same time-step size was used in all simulations. Each computation was initiated with a uniform velocity of (V_{inlet}, 0) in the entire computational domain, and an unsteady simulation was run for 10,000 steps (0.1 s, or approximately 140 periods for $\dot{m} = 267.9$ g/s). Then, the unsteady simulation was run for another 10,000 time steps to record the time statistics, resulting in a total of 20,000 time steps for each simulation. The maximum number of iterations to be performed per time step was set to 20.

The computational mesh was created using the ANSYS Meshing software, and the sensitivity of calculations with respect to grid size was checked to determine the sufficient resolution and grid quality metrics. The mesh parameters are given in Table 3. To achieve mesh independence, the parameters for mesh 1 in Table 3 were successively halved, and four meshes were created. Figure 5 shows a computational mesh for the 2-D NASA hump using the mesh 1 parameters. The final mesh (mesh 4) has 2.6 million elements, with the first 41 layers of the wall stretching at a growth rate of 1.1.

Using the numerical model described previously, unsteady simulations were run for the 2-D NASA hump model using the four computational meshes given in Table 3. As shown in Fig. 6, the turbulent boundary-layer velocity profile at the reference location ($x/c = -2.14$) is compared with the experimental measurements of Greenblatt et al. [29] given at the NASA turbulence resources website [32]. Moreover, the logarithmic law of the wall is included in the figure. The numerical results show a good agreement with the law of the wall and some agreement with the experimental data. The splitter-plate effect was not considered in this simulation. The pressure coefficient C_p over the hump from the unsteady calculations for all the meshes over the hump is plotted in Fig. 7, and experimental data are included for comparison. The time-averaged C_p distributions from the numerical simulations were shifted by -0.03 to better match the experimental reference upstream conditions. The simulation results and experimental data agree well for $x/c < 0.2$. There is a slight increase of C_p for $0.2 < x/c < 0.6$ in all simulations due to the end-plate effect, which is not included in the present study. For $x/c > 0.65$, the results indicate a shift as seen in all RANS simulations [32]. Increasing the grid size did not change the simulation results, indicating that a mesh-independent solution was obtained.

To assess the performance of the SWJ actuator on flow-separation control, the SWJ actuator was integrated into the hump model, and a new computational mesh (HSM3) was created based on the parameters of mesh 3. The number of layers to capture the boundary-layer profiles was reduced to 15, and the maximum face size was increased to 2×10^{-3} m. Figure 8 shows the computational mesh near the SWJ geometry. The mesh shown in Fig. 8 was used throughout the present study to assess the performance of the SWJ actuator running at different flow conditions listed in Table 2.

Table 1 Flow parameters at the inlet boundary of the 2-D NASA wall-mounted hump model

Parameter	Values
M	0.1
Re_c	936,000
P_0	102,036 Pa
T_0	298.93 K

Table 2 Flow parameters at the SWJ actuator inlet boundary

$\dot{m}$, g/s	M	Re_{DH}	P_0, Pa	T_0, K
44.6	0.027	1368	101,826	298.25
89.3	0.052	2738	105,085	298.30
178.6	0.096	5474	114,290	298.86
267.9	0.131	8127	126,613	299.61

Table 3 Mesh parameters

Name	Maximum face size	First layer thickness	Maximum layers	Growth rate	Number of elements
Mesh 1	6.0×10^{-3}	4×10^{-5}	41	1.1	69,722
Mesh 2	3.0×10^{-3}	2×10^{-5}	41	1.1	213,664
Mesh 3	1.5×10^{-3}	1×10^{-5}	41	1.1	724,490
Mesh 4	7.5×10^{-4}	8×10^{-6}	41	1.1	2,626,101
HSM3	2.0×10^{-3}	1×10^{-5}	15	1.1	575,937

III. Results and Discussion

In this section, we performed 2-D URANS simulations for the SWJ actuator integrated to the 2-D NASA wall-mounted hump. An ideal gas was assumed with $\gamma = 1.4$ and $R = 287$ J/(kg · K). The governing equations were discretized in space using a cell-based least-squares finite volume formulation for pressure–velocity coupling. A second-order discretization for pressure and a second-order upwind formulation for density, momentum, turbulent kinetic energy, specific dissipation rate, and energy were adopted. A fully turbulent flow was assumed, and the SST $k-\omega$ model was used in the simulations. A bounded second-order implicit formulation was used for the time-dependent solution formulation. The time-accurate simulations used a constant time step of $\Delta t = 10^{-5}$ s. The maximum number of iterations performed per time step was 20.

In the present 2-D simulations, the mass-flow rate of the SWJ actuator is described as a mass-flux boundary condition. In the literature, it is customary to report the mass-flow rate, and therefore, Table 4 is provided as a reference. The height of the SWJ inlet boundary is 4.0531×10^{-3} m, as shown in Fig. 3c. The SWJ inlet area was calculated assuming a unit depth of 1 m, and mass-flow rates were calculated. The mass fluxes given in Table 4 were used

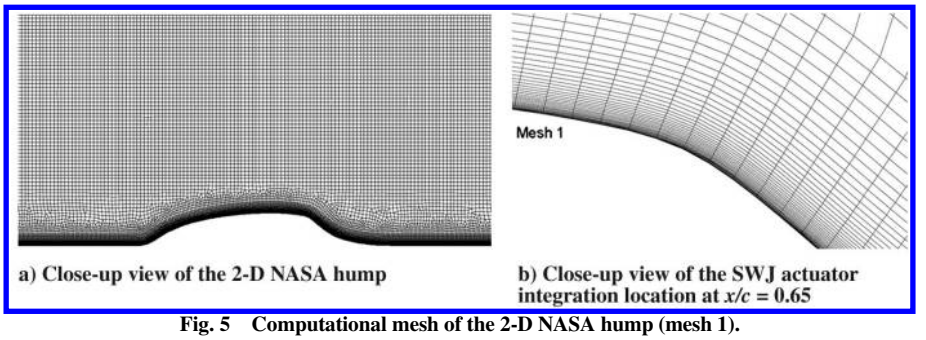

Fig. 5 Computational mesh of the 2-D NASA hump (mesh 1).

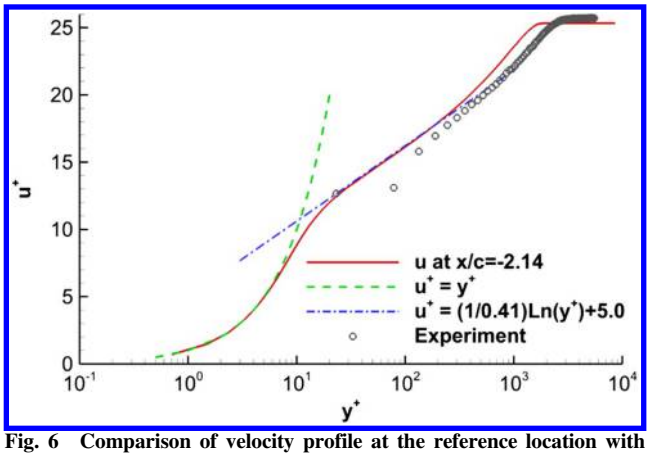

Fig. 6 Comparison of velocity profile at the reference location with experimental measurement.

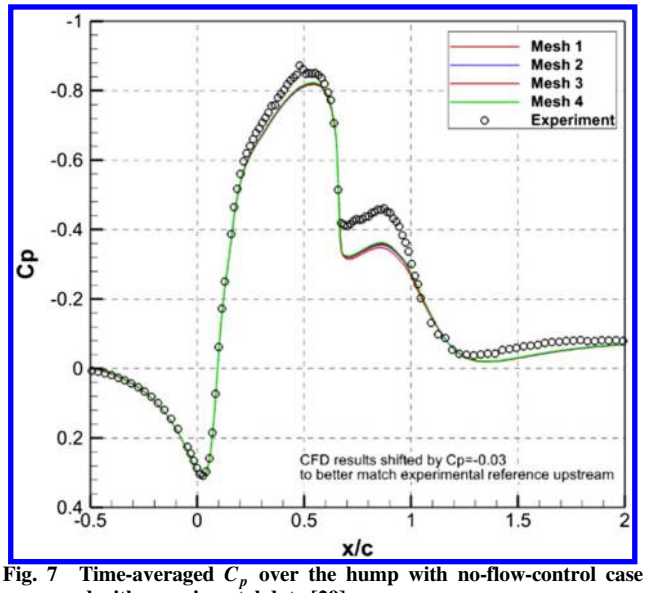

Fig. 7 Time-averaged C_p over the hump with no-flow-control case compared with experimental data [29].

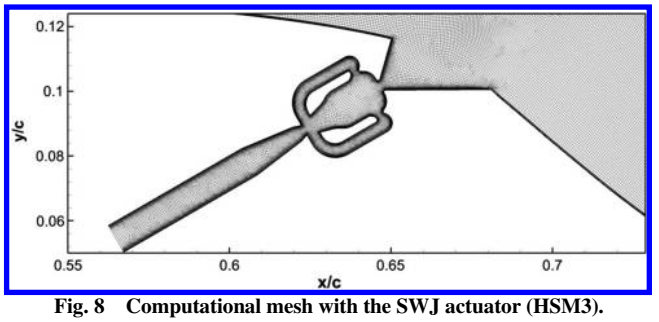

Fig. 8 Computational mesh with the SWJ actuator (HSM3).

Table 4 SWJ actuator mass-flow rates

Mass flux, kg/m^2	$\dot{m}$, g/s	C_μ, %
11.017	44.6	0.4
22.033	89.3	1.4
44.067	178.6	5.7
66.100	267.9	12.8

in our previous studies [22,23]. Using the definition provided in reference [33], a nondimensional momentum coefficient (C_μ) was calculated for better comparison between different configurations. However, for the 2-D configuration used in the present study, the reference area A_{ref} is defined differently as the product of the chord length ($c = 0.42$ m) and the unit depth (1 m). The jet exit velocity was calculated as a result of the mass-flow rate assuming freestream conditions at the actuator exit.

The time history of velocity magnitude was sampled at the downstream of the SWJ exit nozzle ($x/c = 0.654$; $y/c = 0.109$) for each mass-flow rate listed in Table 4, and the results are plotted in Fig. 9a. As shown in the figure, the velocity magnitude was nondimensionalized by a reference velocity of 34.6 m/s. A periodic variation of velocity similar to a square wave is visible, and it is more pronounced at higher mass-flow rates. Because all the simulations were run at the constant time-step size of 1×10^{-5} s, another simulation was performed using 5×10^{-6} s at the highest mass-flow-rate conditions, which also produced the highest jet oscillation

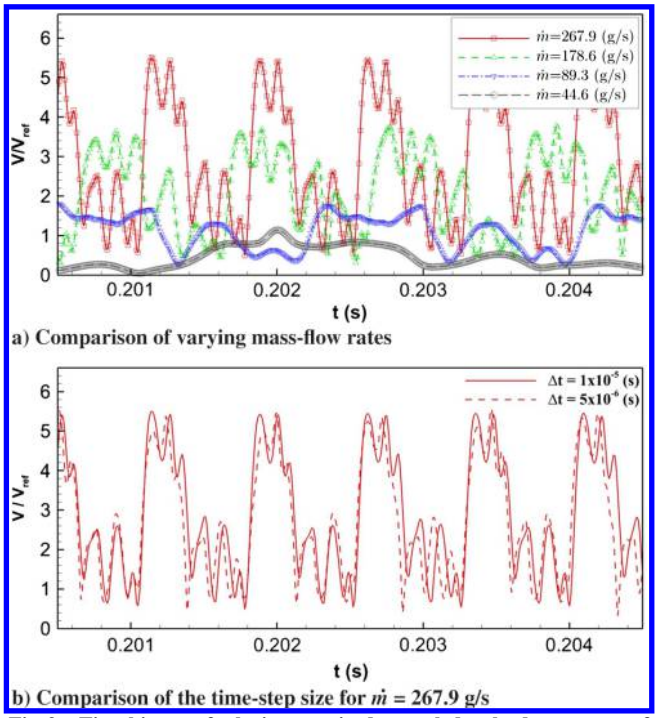

Fig. 9 Time history of velocity magnitude sampled at the downstream of the SWJ actuator exit nozzle.

Table 5 Jet oscillation frequency

$\dot{m}$, g/s	f, Hz
44.6[a]	300
89.3[a]	500
178.6[a]	1001
267.9[a]	1401
267.9[b]	1401

[a]$\Delta t = 1 \times 10^{-5}$ s.
[b]$\Delta t = 5 \times 10^{-6}$ s.

frequency. The comparison of the time history of the velocity magnitude is presented (Fig. 9b), and a very close agreement was observed. The maximum and minimum velocities were very close over the oscillation cycles. However, a slight phase shift was also observed. To find the jet oscillation frequency at every mass-flow rate, a fast Fourier transform (FFT) analysis was performed, and the results are listed in Table 5. The estimated frequency increased with the mass-flow rate linearly ($f = 5.0166\,\dot{m} + 72.61$; $R^2 = 99.77\%$). The frequency analysis of $\dot{m} = 267.9$ g/s case resulted in the same frequency of 1401 Hz for both of the time-step sizes, which indicates the $\Delta t = 1 \times 10^{-5}$ s is adequate to capture the jet oscillation and its frequency.

Snapshots of unsteady simulations are shown in Figs. 10 and 11. Figure 10 shows the instantaneous, mean, and rms velocity magnitude contours around the SWJ actuator operating at a mass-flow rate of 267.9 g/s. Figure 10a shows the jet entering into the SWJ actuator, the jet attachment to the upper wall due to the Coanda effect, and the high-speed jet exiting the SWJ actuator parallel to the freestream. Figure 10b shows the simulation results are averaged over 0.1 s using 10,000 steps, and time-averaged values are calculated. Unlike earlier results of an SWJ actuator in a quiescent environment [21–23], the oscillating jet from the SWJ actuator was biased toward the streamwise direction due to the existence of freestream and asymmetric exit walls, as shown in Fig. 10c. The instantaneous total pressure (Pa gauge, $P_{\text{ref}} = 101{,}325$ Pa) contours inside the SWJ actuator are shown in Fig. 11a. Higher values of total pressure show that the internal jet flow branches in the SWJ actuator core toward feedback channels and the SWJ actuator exit nozzle. A high-speed cooling effect along the jet is visible in Fig. 11b. The Mach number at the SWJ actuator exit nozzle reached up to 0.57, as shown in the instantaneous Mach contours plotted in Fig. 11c for a mass-flow rate of 267.9 g/s, which corresponds to a momentum coefficient of $C_\mu = 4.08\%$.

The total pressure drop inside the SWJ actuator for a mass-flow rate of 178.6 g/s is plotted in Fig. 12 over an oscillation cycle at various phases, as indicated by the time stamps. The contour values were nondimensionalized by the reference pressure of $P_{\text{ref}} = 101{,}235$ Pa. The jet oscillation frequency was calculated as 1 kHz. Snapshots show the various phases of the oscillation process, such as the jet exiting the SWJ actuator (Figs. 12a and 12e) and flow from the feedback channel pushing the jet to the other side (Figs. 12d and 12h). An animation of the jet oscillation can be seen in Supplemental Video S1. Moreover, a set of videos of total pressure drop for the mass-flow rate of 267.9 g/s including the streamlines are provided in Supplemental Videos S2–S5.

Velocity magnitude contours are shown in Fig. 13 for the mass-flow rate of 178.6 g/s. The velocity was nondimensionalized with the reference velocity of $V_{\text{ref}} = 34.6$ m/s. In the FFT analysis, the jet oscillation period was estimated as 1 ms and the phase-locked snapshots were plotted. However, the snapshots seemed to be in phase when the period was set to 1.01 ms, as shown in Fig. 13. The full oscillation cycle of velocity contours and streamlines can be seen

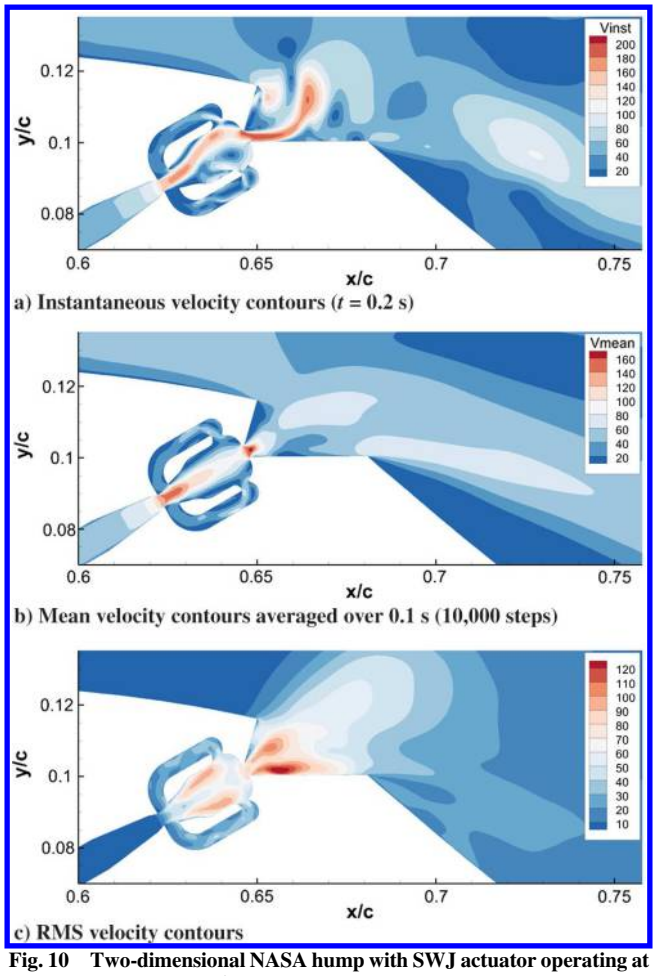

Fig. 10 Two-dimensional NASA hump with SWJ actuator operating at mass-flow rate of 267 g/s ($C_\mu = 4.08\%$); dimension of velocity in meters per second.

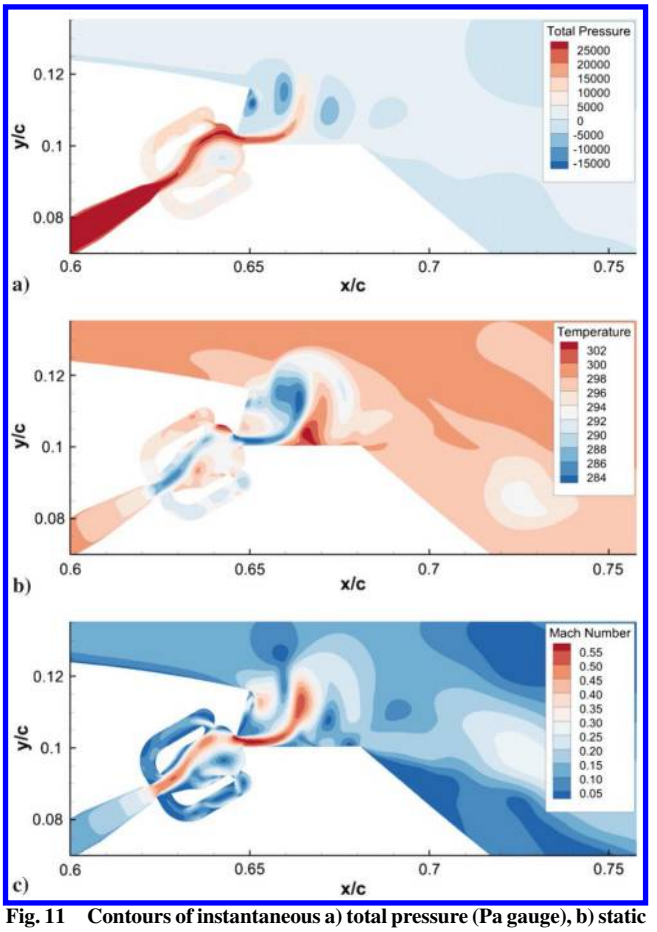

Fig. 11 Contours of instantaneous a) total pressure (Pa gauge), b) static temperature (K), and c) Mach number around the SWJ actuator at a mass-flow rate of 267 g/s ($C_\mu = 4.08\%$).

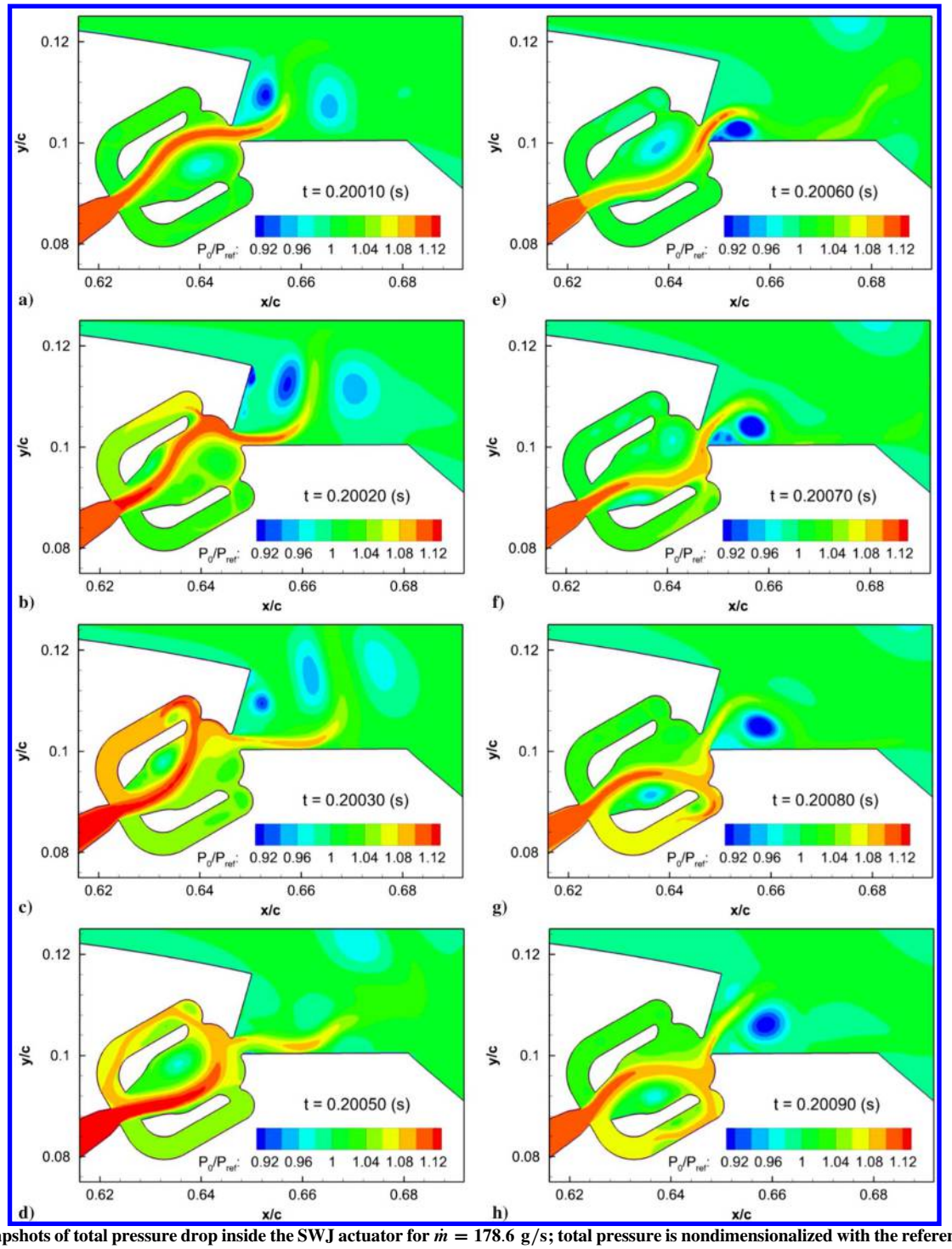

Fig. 12 Snapshots of total pressure drop inside the SWJ actuator for $\dot{m} = 178.6$ g/s; total pressure is nondimensionalized with the reference pressure, $P_{\text{ref}} = 101{,}325$ Pa; jet oscillation frequency is 1 kHz.

in Supplemental Videos S6–S9 for the mass-flow rates of 178.6 and 267.9 g/s.

Figure 14 shows the mean velocity contours superimposed with streamlines that are calculated from the mean velocity components for the mass-flow rates of 0.0, 44.6, 89.3, 178.6, and 267.9 g/s. The reattachment points are extracted from Fig. 14 and summarized in Table 6 along with the nondimensional jet velocity and momentum coefficient C_μ. In the table, the reattachment locations from the 2-D NASA wall-mounted hump separated flow validation case (no plenum) [29,32] are included as a reference. It is provided in Fig. 14a, in which the reattachment occurs at $x/c = 1.25$. In the table, the baseline represents the SWJ actuator integrated wall-mounted hump geometry with no flow control, as shown in Fig. 14b. Because all the RANS models overpredicted the reattachment location, the comparison was made with the baseline result, $x/c = 1.38$. In all of the cases, the separation bubble size was reduced and the reattachment location moved upstream. For the mass-flow rate of 267.9 g/s, the reattachment point moved 41% in the upstream direction. An animation showing the interaction of the oscillating jet and the separation bubble can be seen in Supplemental Video S10. The video file shows that the SWJ actuator was working in two modes and continuously oscillated between them. In the first mode, the jet approached the wall on the left side of the SWJ actuator symmetry axis and injected momentum almost vertically to the incoming flow over the hump. It created a spanwise vortex. Three-dimensional simulations are needed to understand the generation and interaction of these

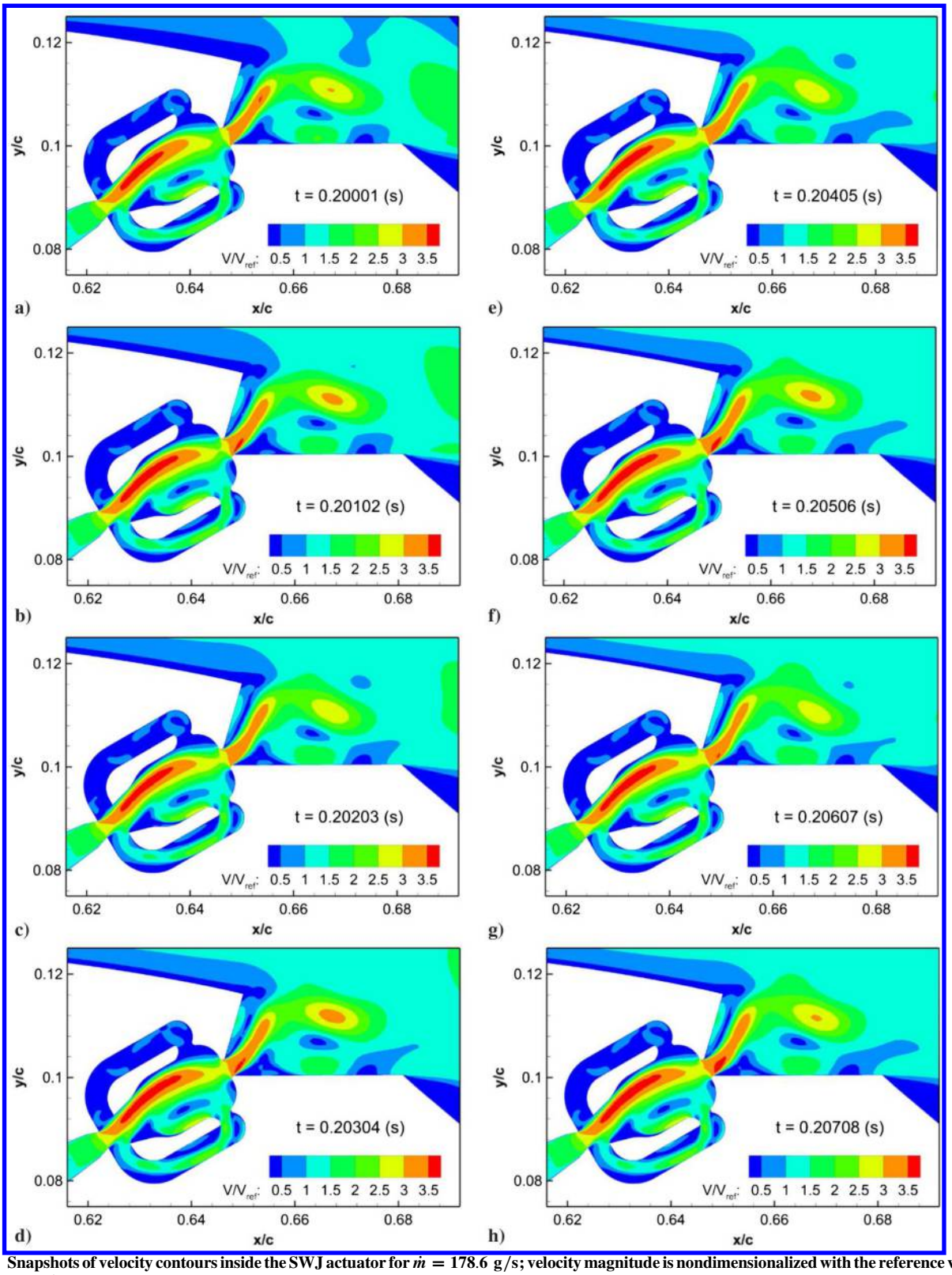

Fig. 13 Snapshots of velocity contours inside the SWJ actuator for $\dot{m} = 178.6$ g/s; velocity magnitude is nondimensionalized with the reference velocity, $V_{\text{ref}} = 34.6$ m/s; jet oscillation frequency is 1 kHz; each snapshot is taken at 1.01 ms apart from each other to get the same phase.

vortical structures fully. In the second mode, the jet approached the wall on the right side of the SWJ actuator symmetry axis and injected momentum parallel to the surface. Moreover, the previously generated spanwise vortex was pushed by the high-speed jet in the downstream direction toward the separation bubble. This interaction attached the flow in the downstream of the SWJ actuator. In both modes, the high-speed jet flow from the SWJ actuator moved between the separation bubble and the low-speed region above, as shown in Fig. 14f.

On the other hand, the addition of the SWJ actuator to the hump model increased the separation bubble size, and it moved the reattachment location 10.4% in the downstream direction from $x/c = 1.25$, as depicted in Figs. 14a and 14b. This can be seen as the penalty of the geometric modification.

The pressure coefficient was calculated from the time-averaged results for various mass-flow rates and is plotted in Fig. 15. Experimental data from reference [29], which was provided by

Table 6 Flow reattachment locations for varying momentum coefficients ($c = 0.42$ m)

$\dot{m}$, g/s	V_{jet}/V_{ref}	C_μ, %	x/c	Relative improvement, %
Baseline (no flow control)[a]	— —	— —	1.38	— —
44.6	0.69	0.4	1.35	2
89.3	1.37	1.4	1.30	6
178.6	2.74	5.7	1.05	24
267.9	4.12	12.8	0.82	41

Note: Relative improvement was calculated using the reattachment location of baseline case without SWJ actuator, $x/c = 1.25$.

[a]Baseline refers to the 2-D NASA wall-mounted hump and integrated SWJ actuator with no flow control. In the 2-D NASA wall-mounted hump experiment, the reattachment location was at $x/c = 1.1$ [29]. CFL3D simulations (SST $k-\omega$; no control) indicated that the reattachment location was at $x/c = 1.25$–1.27 [32].

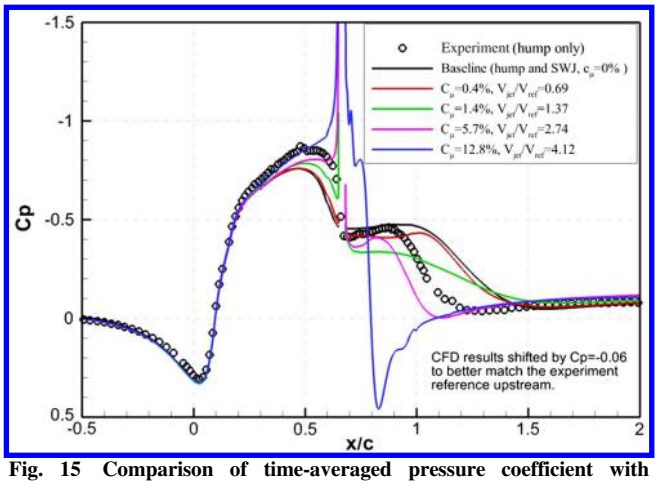

Fig. 15 Comparison of time-averaged pressure coefficient with experimental data [29] for varying SWJ mass-flow rates.

reference [32], are included. The numerical simulation results are shifted by −0.06 to match the experimental reference upstream values. A similar approach was also used in reference [32]. The momentum coefficients and jet-to-reference-velocity ratios are provided for comparison. In Fig. 15, the enlarged separation bubble caused the difference between the baseline result (hump and SWJ with no flow control) and the experimental measurements (hump only). The spike in the C_p distributions for $C_\mu > 1.4\%$ resembles the spike in the inviscid solution given in fig. 12 of Ref. [33], showing the effectiveness of flow control. Furthermore, in the literature, significant differences of the pressure coefficient between three experimental studies [28,29,33] are reported, as shown in fig. 9 of Ref. [33]. After an investigation of several parameters, including local and total blockage corrections, Borgmann et al. [33] concluded that a combination of end-plate effects and incoming boundary-layer behavior is responsible for discrepancies, not the blockage effect. In the present 2-D concept exploration study, the blockage effect was not included, similar to another recent 2-D numerical study by Fisher et al. [34].

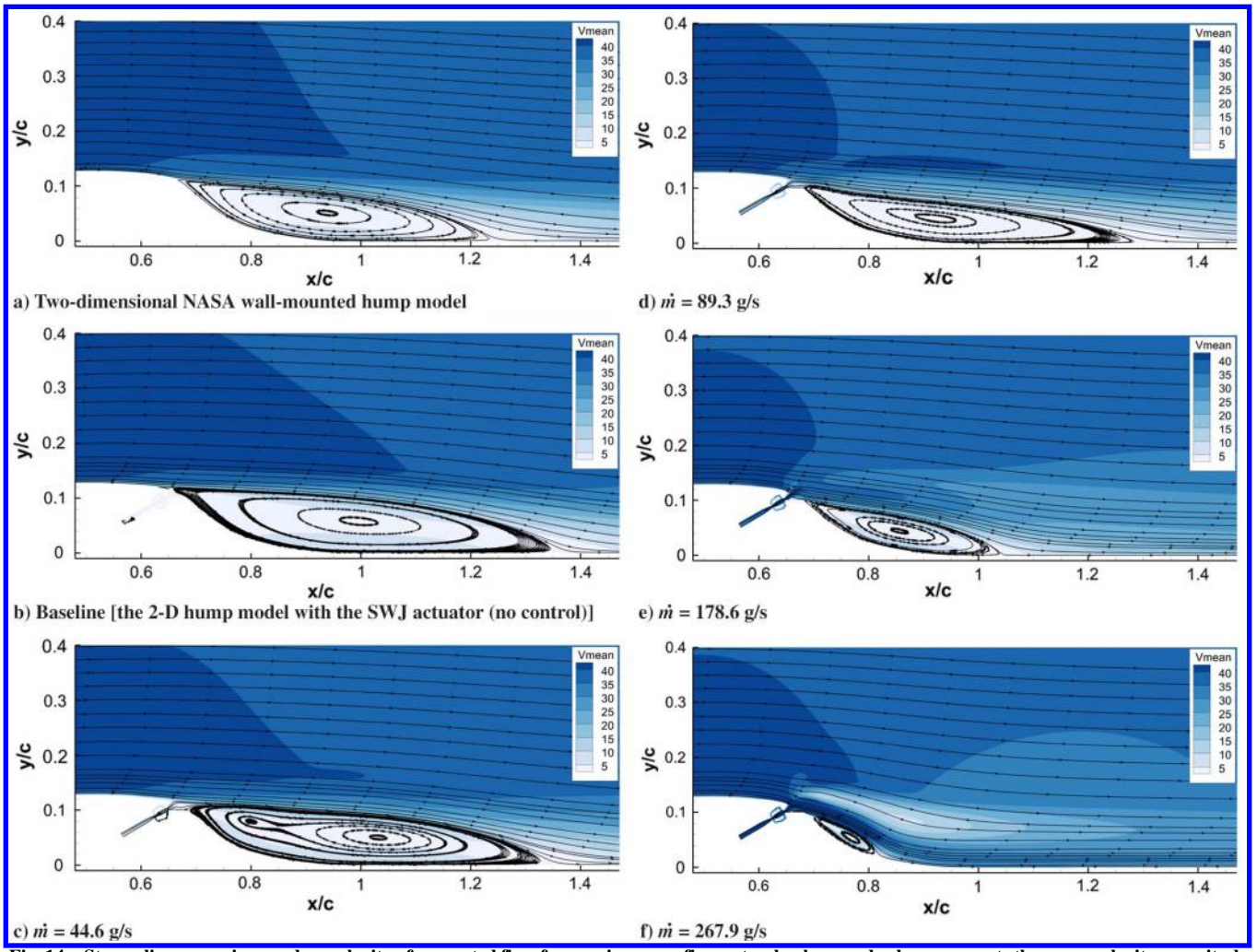

Fig. 14 Streamlines superimposed on velocity of separated flow for varying mass-flow rates; background color represents the mean velocity magnitude (m/s).

IV. Conclusions

In this concept exploration study, a set of 2-D URANS simulations was performed to examine the potential use of an SWJ actuator to reduce flow separation. The simulations were performed for the 2-D NASA hump model with an integrated SWJ actuator configuration to assess the performance of the SWJ actuator compared to the baseline (modified geometry with no flow control) and experimental measurements. A fully turbulent flow was assumed and the SST $k-\omega$ turbulence model was used. Four different mass-flow rates ranging from 44.6 to 267.9 g/s were applied to the SWJ actuator.

One of the main conclusions from this study is that the SWJ actuator reduced the size of the separation bubble in all cases and the reattachment point moved upstream by 41% when operating at $C_\mu = 12.8\%$. The C_p distribution approach to the inviscid solution for $C_\mu > 1.4\%$. It is a clear indication of the effectiveness of flow control. The simulation results suggest that the performance of the SWJ actuator, in terms of decreasing the size of the separation bubble, increases with the mass-flow rate. However, the integration of the SWJ actuator to the hump model moved the reattachment location 8% in the downstream direction.

The present study aimed to make an initial qualitative prediction of the performance of an SWJ actuator on a widely used validation case: the 2-D NASA wall-mounted hump separated flow case. Further investigation of a three-dimensional model and other orientations of the SWJ actuator using higher-fidelity simulations, such as LES or direct numerical simulation, is required to fully understand the detailed flow separation and control mechanisms.

Acknowledgments

The authors would like to acknowledge the Office of Scientific Research of Khalifa University and Khalifa University—Korea Advanced Institute of Science and Technology (KAIST) Institute for the financial support provided.

References

[1] Abbas, A., de Vicente, J., and Valero, E., "Aerodynamic Technologies to Improve Aircraft Performance," *Aerospace Science and Technology*, Vol. 28, No. 1, July 2013, pp. 100–132. doi:10.1016/j.ast.2012.10.008

[2] Cattafesta, L. N., and Sheplak, M., "Actuators for Active Flow Control," *Annual Review of Fluid Mechanics*, Vol. 43, No. 1, Jan. 2011, pp. 247–272. doi:10.1146/annurev-fluid-122109-160634

[3] Raghu, S., "Fluidic Oscillators for Flow Control," *Experiments in Fluids*, Vol. 54, No. 2, Feb. 2013, p. 1455. doi:10.1007/s00348-012-1455-5

[4] Bobusch, B. C., Woszidlo, R., Bergada, J. M., Nayeri, C. N., and Paschereit, C. O., "Experimental Study of the Internal Flow Structures Inside a Fluidic Oscillator," *Experiments in Fluids*, Vol. 54, No. 6, June 2013, p. 1559. doi:10.1007/s00348-013-1559-6

[5] Woszidlo, R., Ostermann, F., Nayeri, C. N., and Paschereit, C. O., "The Time-Resolved Natural Flow Field of a Fluidic Oscillator," *Experiments in Fluids*, Vol. 56, No. 6, June 2015, p. 125. doi:10.1007/s00348-015-1993-8

[6] Tesař, V., Zhong, S., and Rasheed, F., "New Fluidic-Oscillator Concept for Flow-Separation Control," *AIAA Journal*, Vol. 51, No. 2, Feb. 2013, pp. 397–405. doi:10.2514/1.J051791

[7] Kara, K., Gunduz, M. E., Kim, J. W., and Sankar, L. N., "Effects of Circulation Control on Power Production for Large Scale Wind Turbines," *51st AIAA Aerospace Sciences Meeting*, AIAA Paper 2013-1105, Jan. 2013. doi:10.2514/6.2013-1105

[8] Seele, R., Tewes, P., Woszidlo, R., McVeigh, M. A., Lucas, N. J., and Wygnanski, I. J., "Discrete Sweeping Jets as Tools for Improving the Performance of the V-22," *Journal of Aircraft*, Vol. 46, No. 6, Nov. 2009, pp. 2098–2106. doi:10.2514/1.43663

[9] Woszidlo, R., Nawroth, H., Raghu, S., and Wygnanski, I., "Parametric Study of Sweeping Jet Actuators for Separation Control," *5th AIAA Flow Control Conference*, AIAA Paper 2010-4247, June 2010. doi:10.2514/6.2010-4247

[10] Sefcovic, J., and Smith, D., "Proportional Aerodynamic Control of a Swept Divergent Trailing Edge Wing Using Synthetic Jets," *48th AIAA Aerospace Sciences Meeting*, AIAA Paper 2010-0092, Jan. 2010. doi:10.2514/6.2010-92

[11] Woszidlo, R., and Wygnanski, I., "Parameters Governing Separation Control with Sweeping Jet Actuators," *29th AIAA Applied Aerodynamics Conference*, AIAA Paper 2011-3172, June 2011. doi:10.2514/6.2011-3172

[12] Seele, R., Graff, E., Gharib, M., Taubert, L., Lin, J., and Wygnanski, I., "Improving Rudder Effectiveness with Sweeping Jet Actuators," *6th AIAA Flow Control Conference*, AIAA Paper 2012-3244, June 2012. doi:10.2514/6.2012-3244

[13] Seele, R., Graff, E., Lin, J., and Wygnanski, I., "Performance Enhancement of a Vertical Tail Model with Sweeping Jet Actuators," *51st AIAA Aerospace Sciences Meeting*, AIAA Paper 2013-0411, Jan. 2013. doi:10.2514/6.2013-411

[14] Tewes, P., Taubert, L., and Wygnanski, I., "On the Use of Sweeping Jets to Augment the Lift of a Lambda-Wing," *28th AIAA Applied Aerodynamics Conference*, AIAA Paper 2010-4689, June 2010. doi:10.2514/6.2010-4689

[15] Koklu, M., and Owens, L. R., "Flow Separation Control over a Ramp Using Sweeping Jet Actuators," *7th AIAA Flow Control Conference*, AIAA Paper 2014-2367, June 2014. doi:10.2514/6.2014-2367

[16] Ostermann, F., Woszidlo, R., Nayeri, C., and Paschereit, C. O., "The Time-Resolved Flow Field of a Jet Emitted by a Fluidic Oscillator into a Crossflow," *54th AIAA Aerospace Sciences Meeting*, AIAA Paper 2016-0345, Jan. 2016, pp. 1–10. doi:10.2514/6.2016-0345

[17] Ostermann, F., Woszidlo, R., Nayeri, C., and Paschereit, C. O., "Effect of Velocity Ratio on the Flow Field of a Spatially Oscillating Jet in Crossflow," *55th AIAA Aerospace Sciences Meeting*, AIAA Paper 2017-0769, Jan. 2017, pp. 1–12. doi:10.2514/6.2017-0769

[18] Hossain, M. A., Prenter, R., Lundgreen, R. K., Agricola, L., Ameri, A., Gregory, J. W., and Bons, J. P., "Investigation of Crossflow Interaction of an Oscillating Jet," *55th AIAA Aerospace Sciences Meeting*, AIAA Paper 2017-1690, 2017. doi:10.2514/6.2017-1690

[19] Aram, S., Lee, Y., Shan, H., and Vargas, A., "Numerical Analysis of Internal and External Flow Fields of a Fluidic Actuator for Active Flow Control Applications," *Proceedings of the ASME 2017 Fluids Engineering Division Summer Meeting*, American Soc. of Mechanical Engineers, New York, 2017, pp. 1–12. doi:10.1115/FEDSM2017-69046

[20] Koklu, M., and Pack Melton, L. G., "Sweeping Jet Actuator in a Quiescent Environment," *43rd AIAA Fluid Dynamics Conference*, AIAA Paper 2013-2477, June 2013. doi:10.2514/6.2013-2477

[21] Vatsa, V., Koklu, M., and Wygnanski, I., "Numerical Simulation of Fluidic Actuators for Flow Control Applications," *6th AIAA Flow Control Conference*, AIAA Paper 2012-3239, June 2012. doi:10.2514/6.2012-3239

[22] Kara, K., "Numerical Study of Internal Flow Structures in a Sweeping Jet Actuator," *33rd AIAA Applied Aerodynamics Conference*, AIAA Paper 2015-2424, June 2015. doi:10.2514/6.2015-2424

[23] Kara, K., "Numerical Simulation of a Sweeping Jet Actuator," *34th AIAA Applied Aerodynamics Conference*, AIAA Paper 2016-3261, June 2016. doi:10.2514/6.2016-3261

[24] Kara, K., "Flow Separation Control Using Sweeping Jet Actuator," *35th AIAA Applied Aerodynamics Conference*, AIAA Paper 2017-3041, June 2017. doi:10.2514/6.2017-3041

[25] Slupski, B. Z., and Kara, K., "Effects of Geometric Parameters on Performance of Sweeping Jet Actuator," *34th AIAA Applied Aerodynamics Conference*, AIAA Paper 2016-3263, June 2016. doi:10.2514/6.2016-3263

[26] Slupski, B. J., and Kara, K., "Effects of Feedback Channels and Coanda Surfaces on the Performance of Sweeping Jet Actuator," *55th AIAA Aerospace Sciences Meeting*, AIAA Paper 2017-0488, Jan. 2017. doi:10.2514/6.2017-0488

[27] Rumsey, C., "NASA Langley Research Center Workshop on Synthetic Jets and Turbulent Separation Control," March 2004, https://cfdval2004.larc.nasa.gov/case3.html [retrieved 17 April 2018].

[28] Seifert, A., and Pack, L. G., "Active Flow Separation Control on Wall-Mounted Hump at High Reynolds Numbers," *AIAA Journal*, Vol. 40, No. 7, July 2002, pp. 1363–1372. doi:10.2514/2.1796

[29] Greenblatt, D., Paschal, K. B., Yao, C. S., Harris, J., Schaeffler, N. W., and Washburn, A. E., "Experimental Investigation of Separation Control Part 1: Baseline and Steady Suction," *AIAA Journal*, Vol. 44, No. 12, Dec. 2006, pp. 2820–2830. doi:10.2514/1.13817

[30] Greenblatt, D., Paschal, K. B., Chung-Sheng, Y., and Harris, J., "Experimental Investigation of Separation Control Part 2: Zero Mass-Flux Oscillatory Blowing," *AIAA Journal*, Vol. 44, No. 12, Dec. 2006, pp. 2831–2845. doi:10.2514/1.19324

[31] Naughton, J. W., Viken, S. A., and Greenblatt, D., "Skin Friction Measurements on the NASA Hump Model," *AIAA Journal*, Vol. 44, No. 6, June 2006, pp. 1255–1265. doi:10.2514/1.14192

[32] Rumsey, C., "2DWMH: 2D NASA Wall-Mounted Hump Separated Flow Validation Case," *Turbulence Modeling Resource*, 2018, https://turbmodels.larc.nasa.gov/nasahump_val.html [retrieved 8 Oct. 2016].

[33] Borgmann, D., Pande, A., Little, J. C., and Woszidlo, R., "Experimental Study of Discrete Jet Forcing for Flow Separation Control on a Wall Mounted Hump," *55th AIAA Aerospace Sciences Meeting*, AIAA Paper 2017-1450, Jan. 2017. doi:10.2514/6.2017-1450.

[34] Fisher, R., Nishino, T., and Savill, M., "Numerical Analysis of a Bidirectional Synthetic Jet for Active Flow Control," *AIAA Journal*, Vol. 55, No. 3, 2017, pp. 1064–1069. doi:10.2514/1.J055081

[35] Uzun, A., and Malik, M. R., "Wall-Resolved Large-Eddy Simulation of Flow Separation over NASA Wall-Mounted Hump," *55th AIAA Aerospace Sciences Meeting, AIAA SciTech Forum*, AIAA Paper 2017-0538, Jan. 2017. doi:10.2514/6.2017-0538

D. Greenblatt
Associate Editor

This article has been cited by:

1. Kewei Xu, Yan Ren, Gecheng Zha. 2022. Numerical Analysis of Energy Expenditure for Coflow Wall Jet Separation Control. *AIAA Journal* **60**:5, 3267-3285. [Abstract] [Full Text] [PDF] [PDF Plus]
2. Ziyan Li, Yudan Liu, Wenwu Zhou, Shiqi Wang, Xin Wen, Yingzheng Liu. Lift Augmentation Potential of the Circulation Control Wing Driven by Sweeping Jets. *AIAA Journal*, ahead of print1-22. [Abstract] [Full Text] [PDF] [PDF Plus]
3. Pierre-Yves Passaggia, Asamaning Quansah, Nicolas Mazellier, Guy Y. Cornejo Maceda, Azeddine Kourta. 2022. Real-time feedback stall control of an airfoil at large Reynolds numbers using linear genetic programming. *Physics of Fluids* **34**:4, 045108. [Crossref]
4. Ziyan Li, Yudan Liu, Wenwu Zhou, Xin Wen, Yingzheng Liu. 2022. Thermal pollution level reduction by sweeping jet-based enhanced heat dissipation: A numerical study with calibrated Generalized k-ω (GEKO) model. *Applied Thermal Engineering* **204**, 117990. [Crossref]
5. Amir Joulaei, Mahdi Nili-Ahmadabadi, Kyung Chun Kim. 2022. Parametric study of a fluidic oscillator for heat transfer enhancement of a hot plate impinged by a sweeping jet. *Applied Thermal Engineering* **205**, 118051. [Crossref]
6. Mohammad Ja'fari, Artur J. Jaworski, Aldo Rona. 2022. Application of synthetic jet arrays for flow separation control on a circular "hump" model. *Experimental Thermal and Fluid Science* **131**, 110543. [Crossref]
7. Kewei Xu, Yan Ren, Gecheng Zha. Numerical Analysis of Energy Expenditure for Co-Flow Wall Jet Separation Control . [Abstract] [PDF] [PDF Plus]
8. Abdul Raouf Tajik, Kursat Kara, Vladimir Parezanović. 2021. Sensitivity of a fluidic oscillator to modifications of feedback channel and mixing chamber geometry. *Experiments in Fluids* **62**:12. . [Crossref]
9. Zhijun Wu, Wenbo Zhao, Zongjie Hu, Wei Xie, Yufeng Wang, Liguang Li. 2021. Study on the Spray Characteristics and Oscillation Mechanism of a Feedback-Free Internal Impinging Nozzle. *Flow, Turbulence and Combustion* **107**:4, 979-1002. [Crossref]
10. Ryo Hirai, Soshi Kawai. 2021. Analysis and Robust Method for Source-Term Modeling of Vortex Generator. *Journal of Aircraft* **58**:5, 958-970. [Abstract] [Full Text] [PDF] [PDF Plus]
11. Kewei Xu, Yan Ren, Gecheng Zha. Separation Control by Co-Flow Wall Jet . [Abstract] [PDF] [PDF Plus]
12. L. Xia, Y. Hua, J. G. Zheng. 2021. Numerical investigation of flow separation control over an airfoil using fluidic oscillator. *Physics of Fluids* **33**:6, 065107. [Crossref]
13. Victor Maldonado, Nicolas Peralta, Serdar Gorumlu, Wolduamlak Ayele. 2021. On the figure of merit and streamwise flow of a propulsive rotor with synthetic jets. *Aerospace Science and Technology* **113**, 106712. [Crossref]
14. Ziyan LI, Kaiwen ZHOU, Yingzheng LIU, Xin WEN. 2021. Jet sweeping angle control by fluidic oscillators with master-slave designs. *Chinese Journal of Aeronautics* **34**:5, 145-162. [Crossref]
15. H. D. Lim, Zhen Lyu. 2021. Observations of a sweeping jet actuator for flow separation control of a backward-facing ramp. *Physical Review Fluids* **6**:4. . [Crossref]
16. Shady E. Ahmed, Omer San, Kursat Kara, Rami Younis, Adil Rasheed. 2021. Multifidelity computing for coupling full and reduced order models. *PLOS ONE* **16**:2, e0246092. [Crossref]
17. Elias Sundström, Mehmet N. Tomac. 2021. Aeroacoustic Characteristics of a Synchronized Fluidic Oscillator. *Flow, Turbulence and Combustion* **106**:1, 61-77. [Crossref]
18. Shabnam Mohammadshahi, Hadi Samsam-Khayani, Tao Cai, Kyung Chun Kim. 2020. Experimental and numerical study on flow characteristics and heat transfer of an oscillating jet in a channel. *International Journal of Heat and Fluid Flow* **86**, 108701. [Crossref]
19. Hadi Samsam-Khayani, Shabnam Mohammadshahi, Kyung Chun Kim. 2020. Experimental Study on Physical Behavior of Fluidic Oscillator in a Confined Cavity with Sudden Expansion. *Applied Sciences* **10**:23, 8668. [Crossref]
20. A. Amouei, Mousa Farhadi. 2020. Numerical investigation of a fluidic oscillator with resonance channel and vortex amplifier. *Chemical Engineering Research and Design* **164**, 424-436. [Crossref]
21. Mehmet N. Tomac, Charles Farbos de Luzan. 2020. Synchronization of a Pair of Opposed Facing Oscillators in a Side-by-Side Configuration. *International Journal of Heat and Fluid Flow* **84**, 108605. [Crossref]
22. Riya Jethani, M Pranav Nandan Goud, Prayas Bhawalkar, K K Bharadwaj. 2020. Numerical study of sweeping jet actuators. *IOP Conference Series: Materials Science and Engineering* **912**:2, 022013. [Crossref]

23. Brian T. Bohan, Marc D. Polanka. 2020. The Effect of Scale and Working Fluid on Sweeping Jet Frequency and Oscillation Angle. *Journal of Fluids Engineering* **142**:6. . [Crossref]
24. Furkan Oz, Kursat Kara. 2020. Jet Oscillation Frequency Characterization of a Sweeping Jet Actuator. *Fluids* **5**:2, 72. [Crossref]
25. Kewei Xu, Yan Ren, Gecheng Zha. Numerical Investigation of NASA Hump Using Co-flow Jet for Separation Control . [Abstract] [PDF] [PDF Plus]
26. Brian T. Bohan, Marc D. Polanka, James L. Rutledge. 2019. Sweeping Jets Issuing From the Face of a Backward-Facing Step. *Journal of Fluids Engineering* **141**:12. . [Crossref]
27. A. Jafarian Amiri, Mousa Farhadi. 2019. Numerical investigation of a single feedback loop oscillator with two outlet channels. *Chemical Engineering Research and Design* **150**, 206-217. [Crossref]
28. Dong Ju Kim, Seyeong Jeong, Tongil Park, Daegyoum Kim. 2019. Impinging sweeping jet and convective heat transfer on curved surfaces. *International Journal of Heat and Fluid Flow* **79**, 108458. [Crossref]
29. David Greenblatt, Edward A. Whalen, Israel J. Wygnanski. 2019. Introduction to the Flow Control Virtual Collection. *AIAA Journal* **57**:8, 3111-3114. [Citation] [Full Text] [PDF] [PDF Plus]
30. Victor Maldonado, Soham Gupta. 2019. Increasing the power efficiency of rotors at transitional Reynolds numbers with synthetic jet actuators. *Experimental Thermal and Fluid Science* **105**, 356-366. [Crossref]